



Full length article

# Mechanisms of exceptional grain growth and stability in formamidinium lead triiodide thin films for perovskite solar cells

Srinivas K. Yadavalli, Zhenghong Dai, Mingyu Hu, Qingshun Dong, Wenhao Li, Yuan Yuan Zhou, Rashid Zia, Nitin P. Padture\*

School of Engineering, Brown University, Providence, RI 02912, USA

## ARTICLE INFO

### Article History:

Received 17 December 2019

Revised 18 March 2020

Accepted 20 March 2020

Available online 5 May 2020

### Keywords:

Halide perovskite

Thin film

Microstructure

Phase transformation

Solar cell

## ABSTRACT

Pure formamidinium lead triiodide ( $\alpha$ -FAPbI<sub>3</sub>) organic-inorganic halide perovskite (OIHP) semiconductor is very attractive for use as light absorber in the new thin-film perovskite solar cells (PSCs) technology. This is primarily because of its superior thermal stability, more suitable bandgap, and compositional simplicity. However, the existence of the photo-inactive non-perovskite  $\delta$ -FAPbI<sub>3</sub> polymorph ('yellow' phase) is a major hurdle in the path towards the development of  $\alpha$ -FAPbI<sub>3</sub>-based PSCs. Also, there is general consensus that the fine-grained nature of OIHP thin films is detrimental to the environmental stability and performance of the resulting PSCs. In this context, here we take advantage of the polymorphism in FAPbI<sub>3</sub>, and use solvent-vapor-assisted  $\delta$ -to- $\alpha$  phase transformation to induce exceptional grain coarsening (up to 50-fold) in 0.3- $\mu$ m thickness FAPbI<sub>3</sub> thin films, resulting in an unprecedented average grain size of up to  $\sim$ 9  $\mu$ m. The underlying mechanisms are elucidated based on the results from a combination of some key experiments, which involve studying systematically the effects of time, temperature, initial grain size, and solvent polarity index (PI). The ultra-coarse-grained  $\alpha$ -FAPbI<sub>3</sub> thin films show dramatically improved environmental stability over their medium-grained counterparts, which is explained based on grain-boundary density arguments. PSCs made using the ultra-coarse-grained  $\alpha$ -FAPbI<sub>3</sub> thin films have improved photovoltaic (PV) performance, but it is somewhat modest. This is attributed to the underestimation of the effective grain size relevant to photocarrier dynamics.

© 2020 Acta Materialia Inc. Published by Elsevier Ltd. All rights reserved.

## 1. Introduction

Organic-inorganic halide perovskites (OIHPs) have attracted a great deal of attention as light-absorber materials in the new thin-film perovskite solar cells (PSCs) [1–3]. The record power conversion efficiency (PCE) of laboratory-PSCs has rocketed from 3.8% in 2009 [4] to 25.2% in 2019 [5], rivalling that of silicon solar cells. The promise of low-cost, solution-processed PSCs with high efficiencies [6], and their potential impact on the global renewable-energy landscape, is driving the work on PSCs worldwide.

Three-dimensional (3D) OIHPs used in PSCs have the general formula AMX<sub>3</sub>, where the organic cation 'A' is CH<sub>3</sub>NH<sub>3</sub><sup>+</sup> (methylammonium, or MA<sup>+</sup>) or HC(NH<sub>2</sub>)<sub>2</sub><sup>+</sup> (formamidinium, or FA<sup>+</sup>), 'M' is a metal cation such as Pb<sup>2+</sup> or Sn<sup>2+</sup>, and 'X' is a halide anion (I-, Br-, or Cl-) [7,8]. Amongst the simple OIHP compositions,  $\alpha$ -FAPbI<sub>3</sub> is more attractive compared with the more popular MAPbI<sub>3</sub> because of its more suitable bandgap ( $\sim$ 1.45 eV) *vis-à-vis* the Shockley-Queisser limit for maximum achievable PCE in a single-junction PSC, and also its superior thermal stability [9]. However, unlike MAPbI<sub>3</sub>, FAPbI<sub>3</sub> can

co-exist as two polymorphs at room temperature (RT): the desirable OIHP 'black' cubic phase  $\alpha$ -FAPbI<sub>3</sub> (space group  $Pm\bar{3}m$ ) and the undesirable non-perovskite 'yellow' hexagonal phase  $\delta$ -FAPbI<sub>3</sub> (space group  $P6_3/mmc$ ).  $\delta$ -FAPbI<sub>3</sub> is the thermodynamically stable phase at RT, with the  $\delta$ -to- $\alpha$  transformation taking place at  $T_c \sim 77$  °C [10]. Since the phase transformation in thin films is constrained by the substrate, the required kinetics for the  $\delta$ -to- $\alpha$  transformation can only be achieved above 130 °C, which often degrades the thin films [11]. By same token, the  $\alpha$ -FAPbI<sub>3</sub> phase can be retained in the thin film metastably when cooled to RT due to insufficient kinetics [12]. However, the lack of constraint in bulk materials (e.g. single-crystals) [13], and in the case of thin films, exposure to light [14] and/or moisture [15], result in its transformation back to the RT-stable  $\delta$ -phase. To improve the stability of  $\alpha$ -FAPbI<sub>3</sub> phase at RT, it is alloyed with smaller cations such as MA<sup>+</sup> [16] or Cs<sup>+</sup> [17–19]. However, alloying typically results in blue-shift in the bandgap, which is undesirable for single-junction PSCs [20]. Also, alloyed OIHPs have greater chemical complexity and are susceptible to phase-separation, resulting in poor stability [21,22]. In this context, pure  $\alpha$ -FAPbI<sub>3</sub> has regained attention, and approaches, such as nano-confinement [23], surface functionalization [24], grain-boundary functionalization [25,26], and doping [27], have been used recently to stabilize the  $\alpha$ -phase.

\* Corresponding author.

E-mail address: [nitin\\_padture@brown.edu](mailto:nitin_padture@brown.edu) (N.P. Padture).

In this context, here we show that significant coarsening of the grain size of pure  $\alpha$ -FAPbI<sub>3</sub> in thin films is a very effective approach for the environmental stabilization of the  $\alpha$ -phase. This follows from our recent study where we demonstrated the exceptional  $\delta$ -to- $\alpha$  phase-transformation-induced grain growth of fine-grained  $\delta$ -FAPbI<sub>3</sub> to ultra-coarse-grained  $\alpha$ -FAPbI<sub>3</sub> thin films via solvent-vapor annealing [28]. This approach circumvents the grain-growth ‘stagnation’ issue prevalent in thin films, which limits the grain size to about the thickness of the thin film [6,29,30]. Here we elucidate the mechanisms underlying this exceptional grain-growth phenomenon in FAPbI<sub>3</sub> thin films, and demonstrate their improved stability and performance. It is argued that in ultra-coarse-grained  $\alpha$ -FAPbI<sub>3</sub> thin films, the very low density of grain boundaries, reduces the ingress of moisture [31], which is responsible for the improved environmental stability. Also, there is general consensus that coarse-grained OIHP thin films are better for photovoltaic (PV) performance of PSCs because grain boundaries are expected to block photocarriers, serve as recombination sites, and provide pathways for facile ion-migration [6,30,32]. In this context, the PV-performance improvements in PSCs made using the ultra-coarse-grained  $\alpha$ -FAPbI<sub>3</sub> thin films, over their medium-grained counterparts, is also demonstrated. However, the improvements are somewhat modest, which could be attributed to the restriction of photocarriers transport by sub-grain boundaries within the large grains [33,34].

## 2. Experimental procedure

### 2.1. Materials and thin film preparation

FAPbI<sub>3</sub> thin films were prepared using the ‘solvent engineering’ method [35]. The precursor solution was prepared by dissolving FAI (Dyesol, Australia) and PbI<sub>2</sub> (Alfa Aesar, USA) in stoichiometric (1:1) ratio in N-N dimethyl formamide (DMF; Sigma Aldrich, USA) to obtain a 45 wt% solution. The solution was spin-coated at 6,000 rpm for 45 s onto pre-cleaned F-doped tin oxide (FTO) coated glass substrates. At the end of the 6<sup>th</sup> second during spinning, 300  $\mu$ L of anti-solvent chlorobenzene (Sigma Aldrich, USA) was dripped quickly at the center of the film. The films were then allowed to dry at room temperature, and they serve as the base thin films ( $\sim$ 0.3  $\mu$ m thickness) comprising fine-grained ( $\sim$ 0.18  $\mu$ m average grain size,  $d$ ), phase-pure  $\delta$ -FAPbI<sub>3</sub>.

The  $\delta$ -FAPbI<sub>3</sub> base thin films were annealed at 100 °C, while being exposed to dimethyl-sulfoxide (DMSO; Sigma Aldrich, USA) solvent vapor, for various durations (up to 15 min) using a setup shown in Fig. S1 (in Supplementary Material or SM) [28], which is similar to that used by Xiao et al. [36]. Briefly, the substrate with the as-deposited thin film was placed on a pre-heated hotplate, and then a drop (10  $\mu$ L) of the solvent was placed  $\sim$ 2 cm from the closest edge of the substrate on a glass slide. The substrate and the glass slide with the solvent drop were covered immediately with an inverted glass Petri dish. In addition to DMSO, which has a polarity index (PI) value of 7.2, other solvents with lower PI values were also used in separate experiments: N-methyl-2-pyrrolidone (NMP) with PI=6.7 and DMF with PI=6.4 [37]. The drop size of DMSO, NMP (Sigma Aldrich, USA), and DMF was 20  $\mu$ L, with the annealing temperature set at 115 °C to compare the relative transformation rates. Additional experiments were performed using DMSO-solvent vapor at other temperatures (95 °C, 100 °C, 105 °C, 110 °C, and 115 °C). In separate experiments,  $\delta$ -FAPbI<sub>3</sub> intermediate thin films with a larger grain size ( $d$ -0.37  $\mu$ m) were obtained by annealing the  $\delta$ -FAPbI<sub>3</sub> base thin films ( $d$ -0.18  $\mu$ m) in DMF vapor at 95 °C for 5 min, using the same setup as above. Control annealing experiments without any solvent-vapor were also performed (N<sub>2</sub> atmosphere).

All the above experiments were performed inside a N<sub>2</sub>-filled glovebox.

### 2.2. Characterization

X-ray diffraction (XRD) was performed on the top surfaces of the thin films in air using a diffractometer (D8 Discover, Bruker AXS, Germany) with Cu K $\alpha$ 1 radiation ( $\lambda$ =1.5406 Å) to identify the phases present.

A scanning electron microscope (SEM; LEO 1530VP, Carl Zeiss, Germany) was used to observe the top surfaces of the thin films. The average grain sizes ( $d$ ) for the thin films were measured using image analysis (ImageJ software) of the SEM images, where for each specimen, at least 200 grains were used. The naturally occurring grain-boundary grooves were assumed to represent the grain boundaries (*i.e.* not etched). It should be noted that this can result in some over-estimation of the grain size because not all grain boundaries are revealed [6,30,38].

In order to observe the microstructural changes in the  $\delta$ -FAPbI<sub>3</sub> base ( $d$ -0.18  $\mu$ m) thin film during DMSO-solvent-vapor annealing, *in situ* optical microscopy (transmission mode) was carried out at 95 °C, 100 °C, 105 °C, 110 °C, and 115 °C. Images were captured every 0.5 s, and they were merged to prepare videos. The videos were trimmed and speeded up by 8 times for annealing at 95 °C and 105 °C, and by 1.7 times for annealing at 115 °C. The  $\alpha$ -FAPbI<sub>3</sub> nuclei, which have been shown to be single-crystalline in nature [28], are better light absorbers and appear darker in the microscope, compared to the surrounding parent  $\delta$ -FAPbI<sub>3</sub>. The nuclei density over an area of  $\sim$ 0.045 mm<sup>2</sup> from these optical images were estimated using image analysis (ImageJ software).

In order to follow the  $\delta$ -to- $\alpha$  transformation during the DMSO-solvent-vapor annealing (100 °C) of the  $\delta$ -FAPbI<sub>3</sub> base ( $d$ -0.18  $\mu$ m) thin film and capture the occurrence of any transient phase(s), *in situ* XRD experiments were also conducted using the same diffractometer as above, equipped with a heating-stage. The setup built for these experiments is shown in Fig. S2 in SM, where the XRD heating stage was used instead of the hotplate, and an X-ray transparent Kapton-tape enclosure was used instead of the inverted glass Petri dish.

For the quantitative estimation of fraction transformed ( $y$ ) during  $\delta$ -to- $\alpha$  transformation the ratio of the 001  $\alpha$ -phase peak intensity at any given time ( $t$ ) to the intensity of the same peak after complete phase transformation was used. The  $y$  vs.  $t$  curves were fitted using the Johnson-Mehl-Avrami-Kolmogorov (JMAK) equation, which describes empirically the kinetics of a solid-state phase transformation at fixed temperature. JMAK equation is given by: [39]

$$y = 1 - \exp(-Kt^n) \quad (1)$$

where  $y$  is the phase fraction of  $\alpha$ -FAPbI<sub>3</sub>,  $t$  is the time lapsed in the reaction, and  $K$  is a reaction constant quantifying the transformation rate. Avrami exponent,  $n$ , is unique to the FAPbI<sub>3</sub> thin film transformation, and is given by the slope of the  $\ln(\ln(1/(1-y)))$  vs.  $\ln(t)$  plot. For determining  $n$ , the  $\delta$ -FAPbI<sub>3</sub> intermediate ( $d$ -0.37  $\mu$ m) thin film was heat-treated at 145 °C (in N<sub>2</sub>). The larger grain size and the higher temperature afforded sufficient number of data points for an accurate estimation of  $n$ . Subsequently, the values of  $K$  for  $\delta$ -to- $\alpha$  FAPbI<sub>3</sub> transformation under different conditions were estimated by fitting the kinetics data to the JMAK Eq. (1) using that  $n$  value.

### 2.3. Environmental Stability Testing

For environmental stability tests and for fabricating PSCs it was necessary to use thicker ( $\sim$ 0.5  $\mu$ m)  $\alpha$ -FAPbI<sub>3</sub> films to ensure that they are smooth and pinhole-free. (Thinner films ( $\sim$ 0.3  $\mu$ m) used for the grain-growth mechanisms studies above are typically less smooth and they may have pinholes.) Here, the thicker  $\delta$ -FAPbI<sub>3</sub> base thin films were obtained using the Lewis acid-base adduct approach inside the N<sub>2</sub>-filled glovebox [25]. The FAPbI<sub>3</sub> precursor solution (containing 0.172 g of FAI, 0.461 g of PbI<sub>2</sub>, 580 mg of DMF, and 95  $\mu$ L of NMP) was spin-coated at 4000 rpm for 30 s on FTO-coated glass

substrates. At the end of 8<sup>th</sup> second, 130  $\mu\text{L}$  of diethyl ether (Sigma Aldrich, USA) was quickly dripped at the center of the film, and annealed at 90  $^{\circ}\text{C}$  for 1 min. These thicker  $\delta\text{-FAPbI}_3$  base thin film had a smaller  $d\sim 0.08\ \mu\text{m}$ , and they were annealed at 160 $^{\circ}\text{C}$  for 20 min in  $\text{N}_2$  atmosphere to obtain  $\alpha\text{-FAPbI}_3$  thin film with  $d\sim 1.2\ \mu\text{m}$  (medium-grained).  $\alpha\text{-FAPbI}_3$  thin films with  $d\sim 3.5\ \mu\text{m}$  (coarse-grained) or  $d\sim 7.6\ \mu\text{m}$  (ultra-coarse-grained) were obtained by DMSO-solvent-vapor annealing the thicker  $\delta\text{-FAPbI}_3$  base ( $d\sim 0.08\ \mu\text{m}$ ) thin film for 5 min at 120  $^{\circ}\text{C}$  or 100  $^{\circ}\text{C}$ , respectively, followed by a heat-treatment at 160  $^{\circ}\text{C}$  for 15 min (in  $\text{N}_2$  atmosphere) to achieve uniform crystallinity.

These  $\alpha\text{-FAPbI}_3$  thin films of three different grain sizes were tested in a climate chamber (RT, 70% relative humidity (RH)) for 40 h to study the effect of grain size on the rate of  $\delta$ -to- $\alpha$  transformation. A control experiment was also conducted to isolate the effect of moisture, where a  $d\sim 1.2\ \mu\text{m}$   $\alpha\text{-FAPbI}_3$  thin film was exposed to dry air ( $\sim 0\%$  RH) in a dry-box at RT for 40 h. The tested thin films were photographed, and they were characterized using XRD.

#### 2.4. PSCs fabrication and testing

Planar  $n$ - $i$ - $p$  PSCs were fabricated using the following stacking sequence: glass/FTO/SnO<sub>2</sub>/FAPbI<sub>3</sub>/Spiro-OMETAD/Au. FTO-coated glass substrates were patterned by etching with Zn and dilute HCl. The etched substrates were subsequently sonicated in deionized water, ethanol, acetone, and isopropanol. Compact SnO<sub>2</sub> electron-transport layer (ETL) was deposited using a method reported elsewhere [40]. The thicker  $\delta\text{-FAPbI}_3$  base ( $d\sim 0.08\ \mu\text{m}$ ) thin films were deposited using the Lewis acid-base adduct approach discussed in the previous section. These were then DMSO-solvent-vapor annealed at 100  $^{\circ}\text{C}$  for 5 min to obtain ultra-coarse-grained  $\alpha\text{-FAPbI}_3$  thin films ( $d\sim 7.6\ \mu\text{m}$ ), followed by a heat-treatment at 160  $^{\circ}\text{C}$  for 20 min (in  $\text{N}_2$ ). To obtain medium-grained  $\alpha\text{-FAPbI}_3$  thin films ( $d\sim 1.2\ \mu\text{m}$ ), the thicker  $\delta\text{-FAPbI}_3$  base ( $d\sim 0.08\ \mu\text{m}$ ) thin films were annealed at 160  $^{\circ}\text{C}$  for 20 min in  $\text{N}_2$  atmosphere. Subsequently, a hole-transport layer (HTL) was deposited by spin-coating at 3000 rpm for 30 s. The HTL solution was prepared by dissolving 60 mg of 2,2',7,7'-tetrakis, (N,N-dimethoxyphenylamine)-9,9'-spirobifluorene (Spiro-OMETAD, Merck, Germany) in 700  $\mu\text{L}$  of chlorobenzene with the following additives: 22.5  $\mu\text{L}$  of 4-tertbutylpyridine, 15.5  $\mu\text{L}$  of Li bis(trifluoromethylsulfonyl)imide (Li-TFSI) solution (520 mg Li-TFSI in 1 mL acetonitrile), and 12.5  $\mu\text{L}$  of FK 209 [tris(2-(1H-pyrazol-1-yl)-4-tert-butylpyridine)-cobalt(III) tris(bis(trifluoromethylsulfonyl)imide) solution (375 mg FK209 in 1 mL acetonitrile). Finally, an Au electrode was thermally evaporated on top to complete the PSC fabrication.

The current density-voltage ( $J$ - $V$ ) responses of the PSCs were measured using a source meter (2400, Keithley, USA) under simulated one-sun illumination (AM 1.5G, 100  $\text{mW}\cdot\text{cm}^{-2}$ ) which was generated using a Class AAA solar simulator (Oriel Sol3A, Newport, USA) under ambient conditions. The light intensity was calibrated using a standard Si photo-diode. The  $J$ - $V$  curves were obtained between 1.2 V to -0.1 V (reverse scan). For each scan, 130 data points were collected with a 10-ms delay per point. A metal photo mask (0.11  $\text{cm}^2$ ) was utilized to define the active area of the PSCs. The steady-state power conversion efficiency of PSCs was measured by monitoring the stabilized current density output under the maximum-power-point bias voltage (calculated from the reverse scan  $J$ - $V$  curve). The steady-state PCE was calculated using the following equation:  $\text{PCE}(\%) = (J \times V_{\text{oc}}) / (100 \times \text{mW}\cdot\text{cm}^{-2}) \times 100$ . The other PV parameters were also extracted from the  $J$ - $V$  data: open circuit voltage ( $V_{\text{oc}}$ ), short-circuit current ( $J_{\text{sc}}$ ), and fill factor (FF). External quantum efficiency (EQE) spectra of the PSCs was also measured using a quantum efficiency measurement system (IQE-200B, Newport, USA).

### 3. Results

The results from our earlier paper [28] are replotted in Fig. 1A, 1B, and 1C showing indexed XRD patterns of the as-synthesized  $\delta\text{-FAPbI}_3$  base ( $d\sim 0.18\ \mu\text{m}$ ) thin film, after DMSO-solvent-vapor-annealing (100  $^{\circ}\text{C}$ , 15 min) or after  $\text{N}_2$ -annealing (100  $^{\circ}\text{C}$ , 15 min), respectively, confirming the phases. The corresponding top-surface SEM images are also presented in Fig. 1D, 1E, and 1F, showing the dramatic effect of DMSO-solvent-vapor-annealing [28]. The fine-grained ( $d\sim 0.18\ \mu\text{m}$ ) nature of the  $\delta\text{-FAPbI}_3$  base thin film is seen in Fig. 1D, whereas the DMSO-solvent-vapor-annealed  $\alpha\text{-FAPbI}_3$  base thin film has  $d\sim 5.3\ \mu\text{m}$ . Fig. 1C and 1F confirm that  $\text{N}_2$ -annealing results in neither phase transformation nor significant grain growth, respectively.

Using the same  $\delta\text{-FAPbI}_3$  base ( $d\sim 0.18\ \mu\text{m}$ ) thin film as above, Fig. 2 presents results from the experiments aimed at quantifying the effect of temperature on the nucleation and growth of  $\alpha\text{-FAPbI}_3$  in the thin films during DMSO-solvent-vapor annealing. The optical images (transmission) in Fig. 2A, 2B, and 2C are of thin films that were DMSO-solvent-vapor annealed at 95  $^{\circ}\text{C}$  (120 s), 105  $^{\circ}\text{C}$  (33 s), and 115  $^{\circ}\text{C}$  (23 s), respectively, at the onset of nucleation (nuclei area fraction  $\sim 2\%$ ). Fig. 2D, 2E, and 2F show corresponding top-surface SEM images of the fully transformed  $\alpha\text{-FAPbI}_3$  films. Optical-microscope movies M1, M2, and M3 in SM show the evolution of nucleation and growth of  $\alpha\text{-FAPbI}_3$  from the parent  $\delta\text{-FAPbI}_3$  during DMSO-solvent-vapor annealing at 95  $^{\circ}\text{C}$ , 105  $^{\circ}\text{C}$ , and 115  $^{\circ}\text{C}$ , respectively. Fig. 2G plots the nuclei density (at the onset of nucleation) and the corresponding final  $d$  values at the end of DMSO-solvent-vapor annealing as function of the annealing temperature. The inverse relationship between the two is clearly seen in this plot: very low nucleation density ( $\sim 4 \times 10^3\ \#\cdot\text{mm}^{-3}$ ), afforded by the lower annealing temperature (95  $^{\circ}\text{C}$ ), results in the  $\alpha\text{-FAPbI}_3$  thin film with largest  $d\sim 9\ \mu\text{m}$ . This report of exceptional grain growth is unprecedented in the OIHP thin films and PSCs literature.

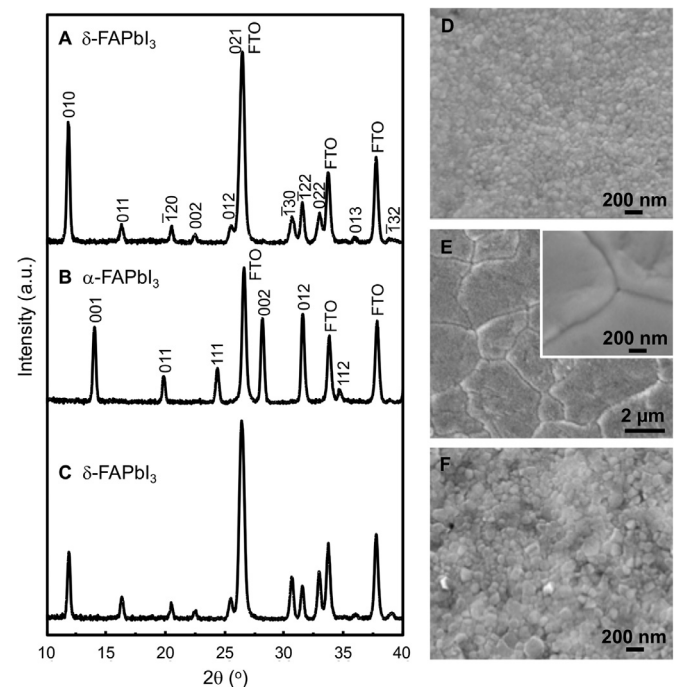


**Fig. 1.** Indexed XRD patterns of: (A) as-synthesized  $\delta\text{-FAPbI}_3$  base ( $d\sim 0.18\ \mu\text{m}$ ) thin film, (B) DMSO-solvent-vapor annealed at 100  $^{\circ}\text{C}$  for 15 min, and (C)  $\text{N}_2$ -annealed at 100  $^{\circ}\text{C}$  for 15 min. Corresponding top-surface SEM images of: (D) as-synthesized  $\delta\text{-FAPbI}_3$  base ( $d\sim 0.18\ \mu\text{m}$ ) thin film, (E) DMSO-solvent-vapor annealed (inset: same magnification as (D) and (F)), and (F)  $\text{N}_2$ -annealed. (Reproduced from Ref. [28] with permission from the American Chemical Society.)

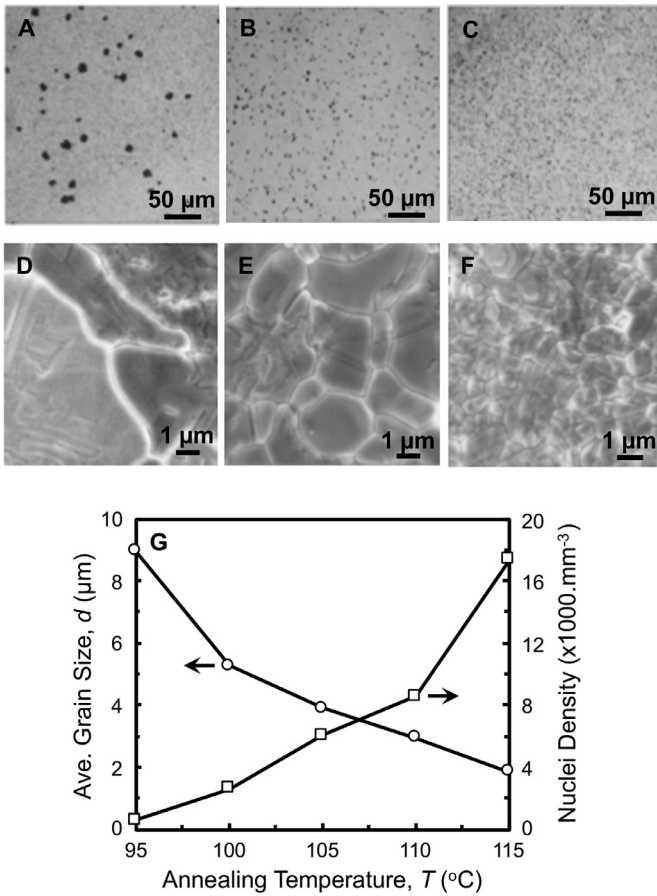


**Fig. 2.** Optical microscope images (transmission) at the onset of  $\alpha$ -FAPbI<sub>3</sub> nucleation in  $\delta$ -FAPbI<sub>3</sub> base ( $d=0.18 \mu\text{m}$ ) thin films during DMSO-solvent-vapor annealing at: (A) 95 °C, (B) 105 °C, and (C) 115 °C. Top-surface SEM images of  $\alpha$ -FAPbI<sub>3</sub> thin films with different grain sizes after DMSO-solvent-vapor annealing the  $\delta$ -FAPbI<sub>3</sub> base ( $d=0.18 \mu\text{m}$ ) thin film for 10 min at: (D) 95 °C, (E) 105 °C, and (F) 115 °C. (G) Nuclei-density of  $\alpha$ -FAPbI<sub>3</sub> at the onset of nucleation and the corresponding average grain size ( $d$ ) of the fully-transformed  $\alpha$ -FAPbI<sub>3</sub> thin films as a function of DMSO-solvent-vapor-annealing temperature.

**Fig. 3** presents the *in situ* XRD results from DMSO-solvent-vapor annealing of the same  $\delta$ -FAPbI<sub>3</sub> base ( $d=0.18 \mu\text{m}$ ) thin film (at 100 °C). The  $\alpha$ -FAPbI<sub>3</sub> ( $2\theta=13.9^\circ$ ) peak starts to appear at  $\sim 2.5$  min, and it

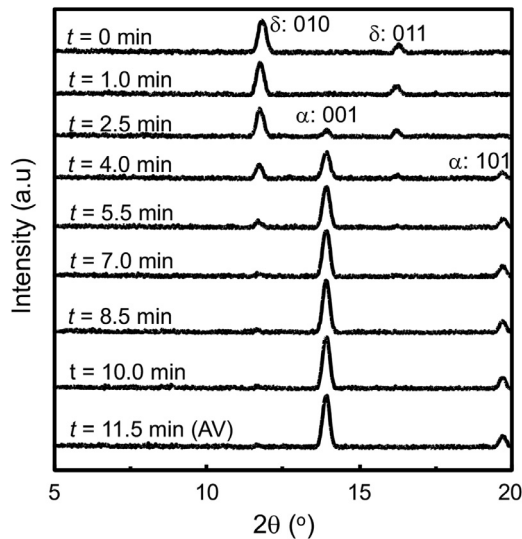


**Fig. 3.** *In situ* indexed XRD patterns at different durations during the DMSO-solvent-vapor annealing of  $\delta$ -FAPbI<sub>3</sub> base ( $d=0.18 \mu\text{m}$ ) thin films at 100 °C. 11.5 min (AV) refers to 1.5 min after venting at the 10<sup>th</sup> min.

grows at the expense of the  $\delta$ -FAPbI<sub>3</sub> ( $2\theta=11.7^\circ$ ) peak. The  $\delta$ -to- $\alpha$  transformation is mostly complete by 7 min. The last XRD pattern in **Fig. 3** is collected 1.5 min after venting the enclosure at the 10<sup>th</sup> min, which does not appear to show any change in the phase composition before and after venting. These *in situ* XRD results confirm the absence of any transient phases and/or crystalline complexes during the DMSO-solvent-vapor annealing. For example, the use of DMSO in the solution processing of OIHP thin films is known to form adduct based intermediate crystalline complexes, such as PbI<sub>2</sub>(DMSO) and PbI<sub>2</sub>(DMSO)<sub>2</sub> with characteristic XRD peaks at  $2\theta=9.8^\circ$  and  $\sim 10.1^\circ$ , respectively [35,41], which are not observed in **Fig. 3**. However, the existence of nanoscale interfacial transient phases at the advancing transformation-front cannot be ruled out.

In order to estimate the Avrami exponent,  $n$ , in the JMAK Eq. (1) for the  $\delta$ -to- $\alpha$  phase transformation in FAPbI<sub>3</sub>, **Fig. 4A** plots the kinetics data (145 °C, N<sub>2</sub> atmosphere) for the starting  $\delta$ -FAPbI<sub>3</sub> intermediate ( $d=0.37 \mu\text{m}$ ) thin film, yielding a slope of  $n\sim 3.6$ . This  $n$  value is slightly on the high side; typically,  $n\sim 3$  for phase transformation in thin films [39]. The reason for this is not clear at this time. **Fig. 4B** presents the  $\delta$ -to- $\alpha$  phase transformation kinetics data for solvent-

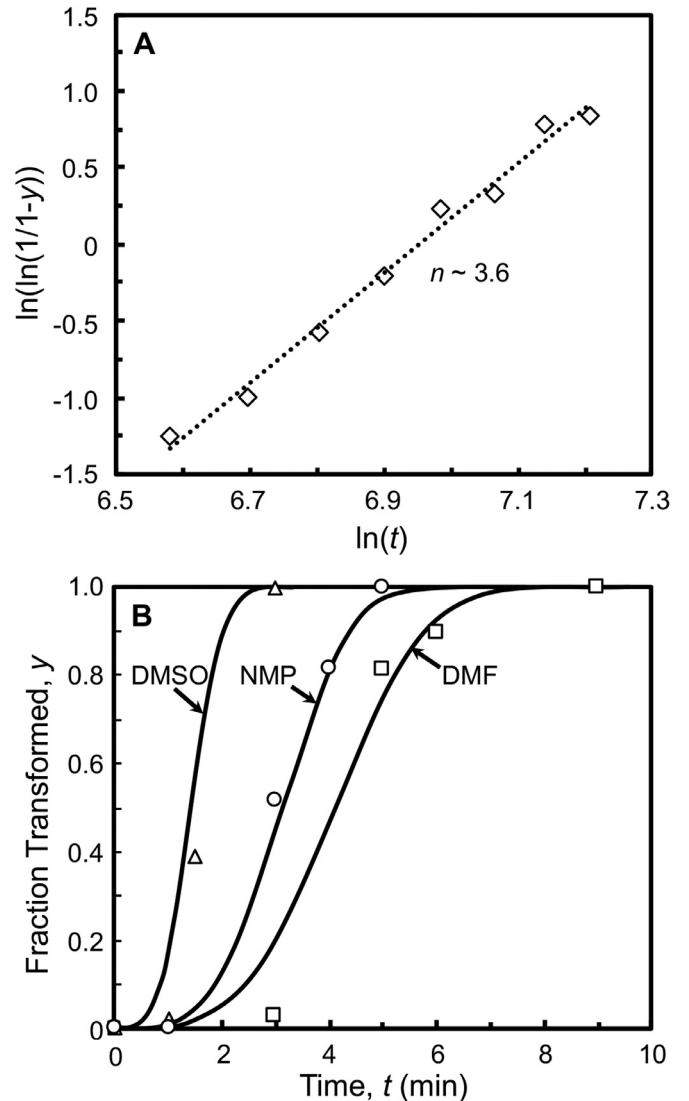


**Fig. 4.** (A) Plot of  $\delta$ -to- $\alpha$  transformation kinetics ( $\ln(\ln(1/(1-y)))$ ) vs.  $t$  for heat-treatment of  $\delta$ -FAPbI<sub>3</sub> intermediate ( $d=0.37 \mu\text{m}$ ) thin film at 145 °C in N<sub>2</sub> atmosphere, and the estimation of the Avrami exponent,  $n\sim 3.6$ . (B) Plots of  $\delta$ -to- $\alpha$  transformation kinetics ( $y$  vs.  $t$ ) data (symbols) for solvent-vapor annealing at 115 °C of  $\delta$ -FAPbI<sub>3</sub> base ( $d=0.18 \mu\text{m}$ ) thin films in DMSO, NMP, and DMF. Solid curves are respective fits to the JMAK model (Eq. (1)) with  $n=3.6$ .

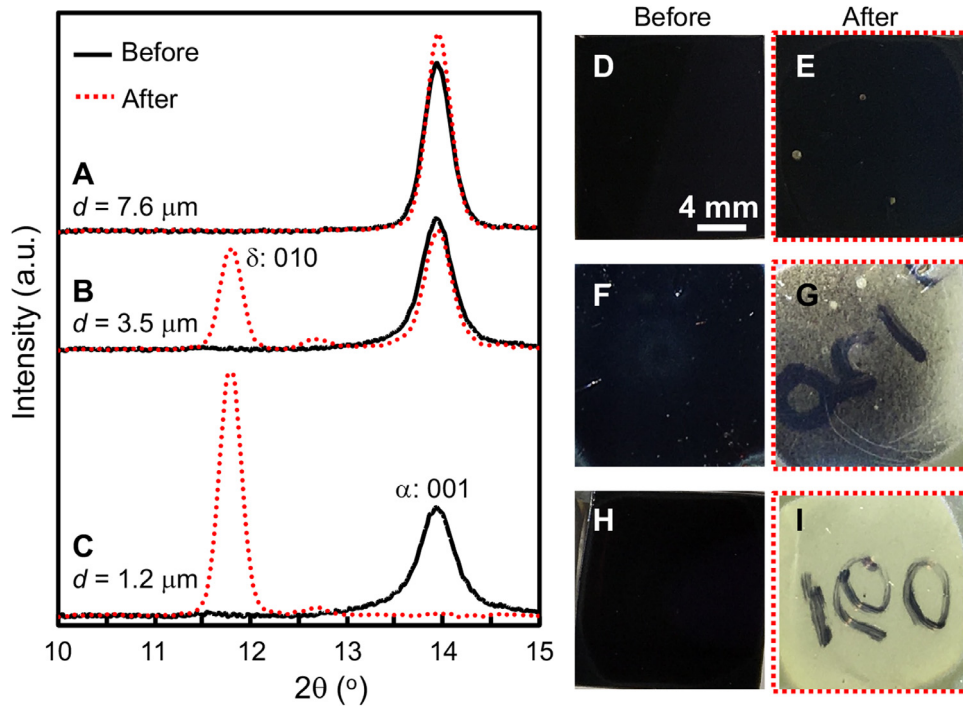


**Fig. 5.** Indexed XRD patterns of  $\alpha$ -FAPbI<sub>3</sub> thin films before and after exposure to 70% RH air at RT for 40 h with average grain sizes: (A)  $d=7.6 \mu\text{m}$ , (B)  $d=3.5 \mu\text{m}$ , and (C)  $d=1.2 \mu\text{m}$ . Corresponding photographs of the  $\alpha$ -FAPbI<sub>3</sub> thin films before and after exposure to 70% RH air at RT for 40 h with average grain sizes: (D,E)  $d=7.6 \mu\text{m}$ , (F,G)  $d=3.5 \mu\text{m}$ , and (H,I)  $d=1.2 \mu\text{m}$ . In (G) and (I), lettering on the bottom of the sample holder is visible due to semi-transparent nature of the degraded ('yellowed') thin film.

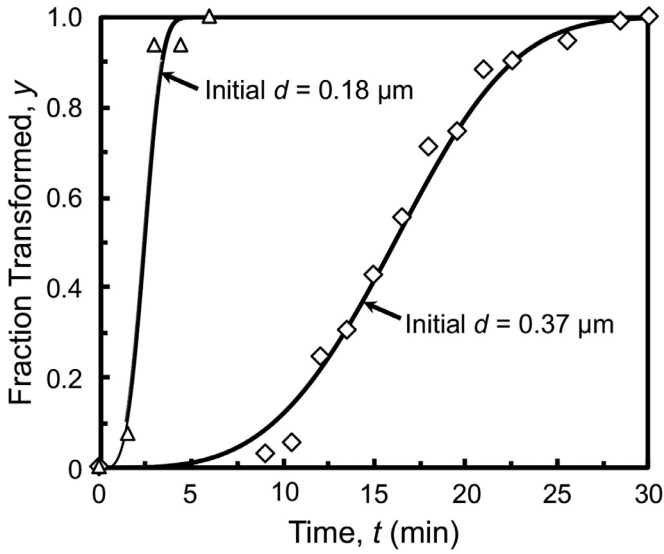
vapor annealing (at 115 °C) of the  $\delta$ -FAPbI<sub>3</sub> base ( $d\sim 0.18 \mu\text{m}$ ) thin films using solvents with different PI values: DMSO (7.2), NMP (6.7), and DMF (6.4). By substituting the value of  $n=3.6$  in Eq. (1), the best-fit (solid curves in Fig. 4B)  $K$  values for annealing under DMSO, NMP, and DMF vapor are determined to be  $8.8 \times 10^{-8}$ ,  $2.1 \times 10^{-9}$ , and  $5.6 \times 10^{-9}$  (units of  $\text{s}^{-3.6}$ ), respectively. It is clear that the use of high-PI solvent-vapor results in faster phase transformation. It is worth noting that Liu et al. [42] found DMSO to be more effective than DMF in the solvent-vapor-annealing grain growth in MAPbI<sub>3</sub> thin films.

In this context, results from our earlier paper on grain growth and phase evolution during DMSO-solvent-vapor annealing at 100 °C are presented in Fig. S3 in SM [28]. The XRD patterns in Fig. S3A–S3D show that in the case of DMSO-solvent-vapor annealing at 100 °C, the  $\delta$ -to- $\alpha$  transformation is complete within 5 min. The SEM image in Fig. S3E shows that the  $\alpha$ -FAPbI<sub>3</sub> film obtained after 5-min annealing has  $d\sim 4.8 \mu\text{m}$ , with the  $\delta$ -FAPbI<sub>3</sub> base thin film (Fig. 1D) having  $d\sim 0.18 \mu\text{m}$ . There is no further grain growth upon extended DMSO-solvent-vapor-annealing (Fig. S3F and S3G). The XRD patterns in Fig. S4A–S4D show that in the case of NMP-solvent-vapor annealing at 100 °C, the  $\delta$ -to- $\alpha$  transformation has barely started at the end of 5 min (Fig. S4A). Also, the grain growth is not as significant in the NMP-solvent-vapor annealing (Fig. S4G), where at the end of 15 min the  $\delta$ -to- $\alpha$  transformation is only partially complete, but  $d$  is  $\sim 1.18 \mu\text{m}$ . The use of higher amount of NMP solvent (20  $\mu\text{L}$ ) did result in complete  $\delta$ -to- $\alpha$  transformation in 15 min (see Fig. S5 in SM). In the case of DMF-solvent-vapor annealing, the XRD patterns (Figs. S6A–S6D) show that the  $\delta$ -to- $\alpha$  transformation has not even started despite 15-min annealing. The grain growth is even less pronounced in the DMF-solvent vapor case (Figs. S6E–S6G), where at the end of 15-min annealing  $d\sim 0.90 \mu\text{m}$  only (Fig. S6G). Significantly higher amount of DMF solvent (60  $\mu\text{L}$ ) is needed to result in complete  $\delta$ -to- $\alpha$  transformation in 60 min (see Fig. S7 in SM). These results confirm that the higher the PI value of the solvent, more effective is the solvent-vapor annealing process in promoting  $\delta$ -to- $\alpha$  transformation and grain growth in FAPbI<sub>3</sub> thin films.

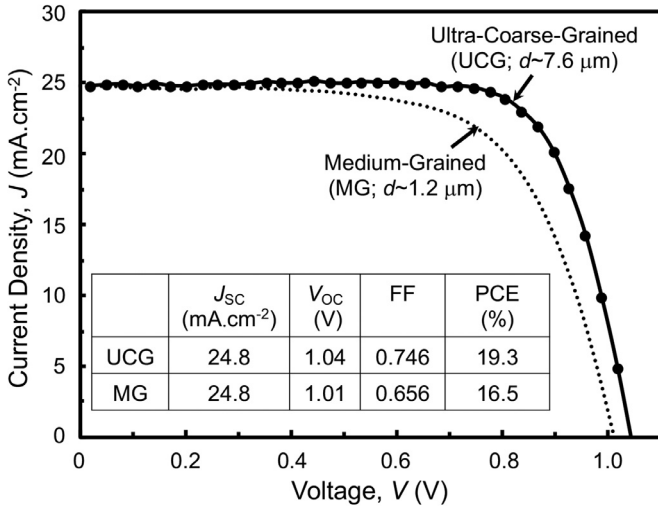
Fig. 5 presents the results comparing  $\alpha$ -phase stability of FAPbI<sub>3</sub> films with different grain sizes. Microstructures of the tested  $\alpha$ -FAPbI<sub>3</sub> thin films shown in Fig. S8A–S8C in SM. XRD patterns in Fig. 5B show that the medium-grained ( $d\sim 1.2 \mu\text{m}$ )  $\alpha$ -FAPbI<sub>3</sub> film has transformed fully to  $\delta$ -FAPbI<sub>3</sub> within 40-h exposure to 70% RH at RT, whereas the coarse-grained ( $d\sim 3.5 \mu\text{m}$ )  $\alpha$ -FAPbI<sub>3</sub> thin film has transformed partially after the same treatment (Fig. 5C). In contrast, the ultra-coarse-grained ( $d\sim 7.6 \mu\text{m}$ )  $\alpha$ -FAPbI<sub>3</sub> thin film (Fig. 5D) remains fully  $\alpha$ -FAPbI<sub>3</sub>. Fig. 5A shows corresponding discoloration ('yellowing') of the films due to the transformation to  $\delta$ -FAPbI<sub>3</sub>. This shows that ultra-coarse-grained  $\alpha$ -FAPbI<sub>3</sub> thin films are significantly more stable than the other thin films with lower  $d$ . This effect has also been observed in MAPbI<sub>3</sub> thin films, but in that case the degradation product is typically PbI<sub>2</sub> [31].

Fig. 6 compares the  $\delta$ -to- $\alpha$  phase transformation kinetics data for  $\delta$ -FAPbI<sub>3</sub> base ( $d\sim 0.18 \mu\text{m}$ ) and intermediate ( $d\sim 0.37 \mu\text{m}$ ) thin films, at 145 °C in N<sub>2</sub> atmosphere. (Fig. S9A and S9B show the microstructures of the  $\delta$ -FAPbI<sub>3</sub> base and intermediate thin films, respectively.) The JMAK Eq. (1) best-fit (solid curves in Fig. 6)  $K$  values for transformation of the base and the intermediate  $\delta$ -FAPbI<sub>3</sub> thin films are  $1.4 \times 10^{-8}$  and  $1.6 \times 10^{-11}$  (units of  $\text{s}^{-3.6}$ ), respectively ( $n=3.6$ ), showing clearly that the starting  $\delta$ -FAPbI<sub>3</sub> thin films with the coarser grains exhibit much slower transformation kinetics. These results highlight the critical role played by grain boundaries in the  $\delta$ -to- $\alpha$  phase transformation.

Fig. 7 shows the  $J$ - $V$  responses and the corresponding PV parameters of the 'champion' PSCs made using medium-grained ( $d\sim 1.2 \mu\text{m}$ ) and ultra-coarse-grained ( $d\sim 7.6 \mu\text{m}$ )  $\alpha$ -FAPbI<sub>3</sub> thin films. The medium-grained PSC has  $J_{\text{SC}}$  of 24.8  $\text{mA}\cdot\text{cm}^{-2}$ ,  $V_{\text{OC}}$  of 1.01 V, FF of 0.656, and PCE of 16.5%. Whereas the ultra-coarse-grained PSC shows improved PV performance, with  $V_{\text{OC}}$  of 1.04 V, FF of 0.746, and PCE of 19.3%, while the  $J_{\text{SC}}$  is the same (24.8  $\text{mA}\cdot\text{cm}^{-2}$ ). Tables S1 and S2 summarize the PV parameters from 20 medium-grained and ultra-coarse-grained PSCs each, with average PCEs of  $15.2\pm 0.9\%$  and  $16.8\pm 1.3\%$ , respectively. Fig. S10 in SM presents EQE spectrum from a PSC (different device from Fig. 7), confirming the high integrated  $J_{\text{SC}}$ .



**Fig. 6.** Fraction of  $\delta$ -FAPbI<sub>3</sub> transformed to  $\alpha$ -FAPbI<sub>3</sub> as a function of reaction time, upon annealing at 145 °C in N<sub>2</sub> atmosphere thin film for  $\delta$ -FAPbI<sub>3</sub> base ( $d$ -0.18  $\mu$ m) and intermediate ( $d$ -0.37  $\mu$ m) thin films.



**Fig. 7.**  $J$ - $V$  characteristics for the 'champion' PSCs incorporating medium-grained ( $d$ -1.2  $\mu$ m) and ultra-coarse-grained ( $d$ -7.6  $\mu$ m)  $\alpha$ -FAPbI<sub>3</sub> thin films. Inset: PV parameters extracted from the  $J$ - $V$  curves.

#### 4. Discussion

The results reported above show clearly that DMSO-solvent-vapor molecules interact with  $\delta$ -FAPbI<sub>3</sub> thin films in a unique way in facilitating their rapid transformation to  $\alpha$ -FAPbI<sub>3</sub> OIHP thin films, with concomitant exceptional grain growth. In order to understand this interesting phenomenon, it is instructive to look at the nature of the  $\delta$ -to- $\alpha$  transformation in FAPbI<sub>3</sub>. The crystal structures of the  $\delta$ -FAPbI<sub>3</sub> (hexagonal, space group  $P6_3/mmc$ ) and the  $\alpha$ -FAPbI<sub>3</sub> (cubic, space group  $P6_3/mmc$ ) are not related through a simple group/subgroup relation [10]. Therefore, the  $\delta$ -to- $\alpha$  polymorphic transformation is reconstructive in nature, where the FA<sup>+</sup>, Pb<sup>2+</sup>, and I<sup>-</sup> ions must undergo a complex combination of sliding and twisting involving thermally-activated breakage and reformation of bonds [10]. This is because the main structural reconstruction in the  $\delta$ -to- $\alpha$  transformation is the change from face-shared (PbI<sub>6</sub>)<sup>4-</sup> octahedra in  $\delta$ -FAPbI<sub>3</sub> to corner-shared (PbI<sub>6</sub>)<sup>4-</sup> octahedra in  $\alpha$ -FAPbI<sub>3</sub>. Since this transformation is composition-invariant, only short-range thermally-activated attachment and detachment of atomic/molecular species across the

$\delta$ - $\alpha$  interface are needed. Detailed *in situ* neutron diffraction studies have shown that during slow heating,  $\delta$ -FAPbI<sub>3</sub> transforms to  $\alpha$ -FAPbI<sub>3</sub> at  $\sim$ 77 °C [10]. (Note that the higher annealing temperatures were chosen in our study to provide sufficient superheating and thermodynamic driving force for the  $\delta$ -to- $\alpha$  transformation to occur within a reasonable timeframe.) However, during slow cooling, the  $\alpha$ -to- $\delta$  reverse transformation occurs at  $\sim$ 17 °C, and it can be kinetically suppressed to much lower temperatures by quenching [10]. Such hysteresis and kinetic suppression indicates the existence of a significant activation-energy barrier between the two states. This is perhaps why, in N<sub>2</sub> atmosphere,  $\delta$ -FAPbI<sub>3</sub> does not transform to  $\alpha$ -FAPbI<sub>3</sub> OIHP in 15 min at 100 °C. Prolonged annealing (120 h) in N<sub>2</sub> atmosphere at 100 °C does result in the  $\delta$ -to- $\alpha$  transformation, but it results in the thermal degradation of the thin film to PbI<sub>2</sub>, as shown in Fig. S11 in SM.

The rate of detachment of the atomic/molecular species from the  $\delta$ -FAPbI<sub>3</sub> parent phase and attachment to the  $\alpha$ -FAPbI<sub>3</sub> OIHP phase across the  $\delta$ - $\alpha$  interface is facilitated by thermal vibrations, and it dictates the transformation kinetics. However, any other forces that influence the detachment/attachment dynamics can also facilitate the transformation of  $\delta$ -FAPbI<sub>3</sub> to the thermodynamically stable  $\alpha$ -FAPbI<sub>3</sub> OIHP phase at the relevant temperature. In this context, strong van der Waals interactions between DMSO, an aprotic polar solvent, and the (PbI<sub>6</sub>)<sup>4-</sup> octahedra has been widely reported in the literature, which can even result in the formation of crystalline complexes such as PbI<sub>2</sub>(DMSO) and PbI<sub>2</sub>(DMSO)<sub>2</sub> [10,16]. Thus, it is expected that during DMSO-solvent-vapor annealing at 95-115 °C, the DMSO molecules in the vapor phase interact strongly with the  $\delta$ -FAPbI<sub>3</sub> phase and help lower the activation-energy barrier for the detachment/attachment process. This occurs without the formation of adduct-based intermediate crystalline complexes, as confirmed by the *in situ* XRD studies (Fig. 3).

Thus, it is logical that a decrease in the polarity of the solvent molecule, as quantified by its PI value, should decrease the effectiveness of its interaction with the  $\delta$ -FAPbI<sub>3</sub> phase. The kinetics data presented in Fig. 4 support this hypothesis, where the order of effectiveness of the solvent-vapor in promoting  $\delta$ -to- $\alpha$  transformation kinetics and the order of their respective PI values are consistent: DMF (6.4) < NMP (6.7) < DMSO (7.2). While those experiments were performed at a fixed temperature ( $T$ =115 °C) for comparing the kinetics, the boiling points (BPs) of the three solvents are different: DMF (153 °C,  $T/T_{BP}$ =0.75), NMP (202 °C,  $T/T_{BP}$ =0.57), and DMSO (189 °C,  $T/T_{BP}$ =0.61) [43]. Therefore, the partial pressure of solvent-vapor of these solvents at 115 °C are also likely to be different. However, it is found that DMSO, with its higher BP compared with DMF, is still relatively more effective. And, NMP with its higher BP compared to DMF, is also found to be relatively more effective. This comparison indicates that the PI-value dominates over the solvent-vapor partial pressure or  $T/T_{BP}$ . Thus, it is reasonable to allow slightly different solvent-vapor partial pressures while comparing the transformation kinetics at a fixed temperature for comparison purposes.

Composition-invariant polymorphic phase transformation in the solid-state typically goes through the processes of nucleation and growth. With regards to nucleation, it is highly likely that the heterogenous nucleation of new  $\alpha$ -FAPbI<sub>3</sub> phase occurs at grain boundaries of the fine-grained parent  $\delta$ -FAPbI<sub>3</sub>. Thus, the activation barrier for nucleation is given by: [44]

$$\Delta G_{\text{Het}}^* = \frac{16A\pi\gamma_{\delta-\alpha}^3}{3(\Delta G_V - \Delta G_S)^2}, \quad (2)$$

where  $\gamma_{\delta-\alpha}$  is the energy per unit area associated with the  $\delta$ - $\alpha$  interface, and  $\Delta G_V$  is the reduction in the free energy per unit volume, which is the thermodynamic driving force for the transformation (Fig. 8A), and it depends on the superheating.  $A$  is a geometrical term describing the nature of the heterogeneous nucleus at the grain

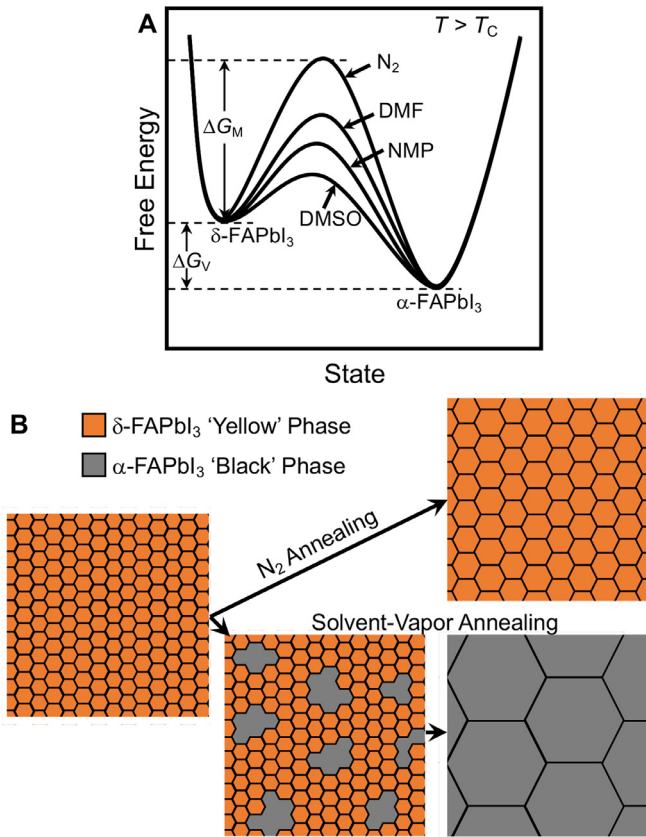


**Fig. 8.** (A) Schematic illustration showing reduction in activation energies for  $\delta$ -to- $\alpha$  phase transformation in FAPbI<sub>3</sub> (relative to N<sub>2</sub>) due to solvent-vapor: DMF, DMSO, and NMP at a temperature above the transformation temperature  $T_c$ . The driving force is  $\Delta G_V$ , and  $\Delta G_M$  is the activation energy. (B) Schematic illustration depicting the mechanism of the solvent-vapor-induced grain growth in FAPbI<sub>3</sub>. (Adapted from ref. 28 with permission from the American Chemical Society.)

boundary and  $\Delta G_S$  is the change in the strain energy per unit volume. The latter becomes important if there is a significant volume strain ( $\Delta V/V$ ) associated with the phase transformation. In the case of FAPbI<sub>3</sub>, the formula-unit volumes of  $\delta$ -FAPbI<sub>3</sub> and  $\alpha$ -FAPbI<sub>3</sub> phases are 256.64 Å<sup>3</sup> and 257.51 Å<sup>3</sup>, respectively [45], resulting in a very small volume strain of -0.34%. However, there is significant strain anisotropy associated with the  $\delta$ -to- $\alpha$  transformation: 3.8% expansion in  $a$  and  $b$  directions, but 7.6% shrinkage in the  $c$  direction. Since the coarse  $\alpha$ -FAPbI<sub>3</sub> nuclei are essentially single-crystal [28], growing at the expense of the fine-grained  $\delta$ -FAPbI<sub>3</sub> parent phase with randomly oriented grains, the  $\Delta G_S$  term becomes important. This is also possibly responsible for the thermal hysteresis in the  $\delta$ -to- $\alpha$  transformation reported by Chen et al. [10]

The nucleation rate is then given by: [44]

$$N_{\text{Het}} \approx B \exp\left(\frac{-\Delta G_M}{kT}\right) \exp\left(\frac{-\Delta G_{\text{Het}}^*}{kT}\right), \quad (2)$$

where  $B$  is a constant and  $\Delta G_M$  is the activation barrier for atomic/molecular detachment/attachment across the  $\delta$ - $\alpha$  interface. The trend in the temperature dependence of the nuclei density (at the onset of nucleation) in Fig. 2, and movies M1, M2, and M3 in SM, are consistent with Eq. (2). Also,  $\Delta G_M$  is expected to be reduced by the solvent-vapor, in the order DMF > NMP > DMSO, as shown schematically in Fig. 8A. Once stable nuclei are formed, their growth is governed by the thermally-activated process given by: [44]

$$G \approx C \exp\left(\frac{-\Delta G_M}{kT}\right) \left[1 - \exp\left(\frac{-\Delta G_{\text{Het}}^*}{kT}\right)\right], \quad (3)$$

where  $C$  is a constant. As seen in Fig. 2, the low nuclei density for the thin films annealed at 100 °C in DMSO-solvent vapor allows the single-crystal nuclei to grow rapidly into large  $\alpha$ -FAPbI<sub>3</sub> OIHP grains, as depicted schematically in Fig. 8B. In the case of nucleation, the growth of the nuclei is also facilitated by the reduction of  $\Delta G_M$  in DMSO-solvent-vapor environment. This is supported by results from an additional experiment that was performed, where a  $\delta$ -FAPbI<sub>3</sub> base ( $d \sim 0.18 \mu\text{m}$ ) thin film was first annealed in DMSO-solvent vapor at 100 °C for 2.5 min (see Fig. S12 in SM) to initiate nucleation of  $\alpha$ -FAPbI<sub>3</sub>. This was followed by N<sub>2</sub>-atmosphere annealing at the same temperature for additional 12.5 min (total 15-min annealing). Results from the SEM and XRD characterization of that film are presented in Figs. S12A and S12B, respectively in SM, which show no further phase transformation or growth of the  $\alpha$ -FAPbI<sub>3</sub> nuclei during the N<sub>2</sub>-atmosphere annealing. In contrast, recall that 15-min annealing at 100 °C in DMSO solvent-vapor results in complete  $\delta$ -to- $\alpha$  transformation and  $d \sim 5.3 \mu\text{m}$  (Fig. 1B and 1E).

As shown in Fig. 2, and depicted schematically in Fig. 8B, low nuclei density is essential for the growth of large  $\alpha$ -FAPbI<sub>3</sub> grains, because the few growing  $\alpha$ -FAPbI<sub>3</sub> nuclei consume the surrounding  $\delta$ -FAPbI<sub>3</sub> matrix in the solid state, without affecting the thickness of the thin film significantly. It is worth noting that, in contrast, OIHP thin films grown from precursor-solution or liquid films, low nuclei density is not desirable because those processes are nutrient-limited, where the few nuclei growing from the solution or liquid not only grow laterally but also vertically (Volmer-Weber growth) [6,30]. Eventually, the precursor or liquid is completely depleted of the OIHP nutrients, resulting in incomplete coverage [6,30].

As mentioned earlier, the kinetics of the  $\delta$ -to- $\alpha$  phase transformation in FAPbI<sub>3</sub> are governed by the rate of detachment of molecular species in the parent phase and the attachment in the product phase. Thus, the high defect density at the grain boundaries of the parent phase is likely to enhance the phase-transformation kinetics. The results presented in Fig. 6 corroborate this hypothesis, where an increase in the  $\delta$ -to- $\alpha$  phase transformation rate is observed with a decrease in the initial  $d$  value (increase in the grain-boundary density) of the parent  $\delta$ -FAPbI<sub>3</sub> phase. In the case of  $\alpha$ -to- $\delta$  reverse phase transformation during the RT environmental exposure, a significantly higher resistance is observed with an increase in the grain size (Fig. 5). This is consistent with what is known in the field: sub-micron grain size  $\alpha$ -FAPbI<sub>3</sub> thin films processed through conventional solution processing routes typically exhibit poor  $\alpha$ -phase stability. This indicates that, while grain boundaries terminating at the surface in a thin film are narrow channels that are exposed to humid environment, as compared to the vast grain surface, they have an out-sized, potent effect on the stability of  $\alpha$ -FAPbI<sub>3</sub>. To put this in perspective, the exposed grain-boundary area, relative to unit grain-surface area exposed, in  $d \sim 1.2 \mu\text{m}$ ,  $d \sim 3.5 \mu\text{m}$ , and  $d \sim 7.6 \mu\text{m}$   $\alpha$ -FAPbI<sub>3</sub> thin films is estimated at  $3.3 \times 10^{-3}$ ,  $1.1 \times 10^{-3}$ , and  $5.2 \times 10^{-4}$ , respectively. This is assuming idealized 2D equiaxed hexagonal grains and 2 nm grain-boundary thickness, with the grain-boundary density (length per unit area) scaling as  $2/d$ .

It is hypothesized that the grain-boundary channels provide pathway for polar H<sub>2</sub>O molecules from the humid environment to ingress into the thin film preferentially over the vast grain surfaces [31]. Since H<sub>2</sub>O is highly polar (PI=10.2 [37]), it is expected to be very effective in facilitating the nucleation of the stable  $\delta$ -FAPbI<sub>3</sub> at RT at the grain boundaries, as shown schematically in Fig. 9. Results from the control experiment (Fig. S13 in SM) in dry air (RT, 40 h), where no  $\alpha$ -to- $\delta$  reverse phase transformation is observed, support this hypothesis. Subsequently, the  $\delta$ -FAPbI<sub>3</sub> nuclei are expected to grow outwards, consuming the bulk  $\alpha$ -FAPbI<sub>3</sub> grains, albeit relatively slowly due to the slow kinetics at RT. However, the complete  $\alpha$ -to- $\delta$  transformation is expected to occur much sooner in the fine-grained

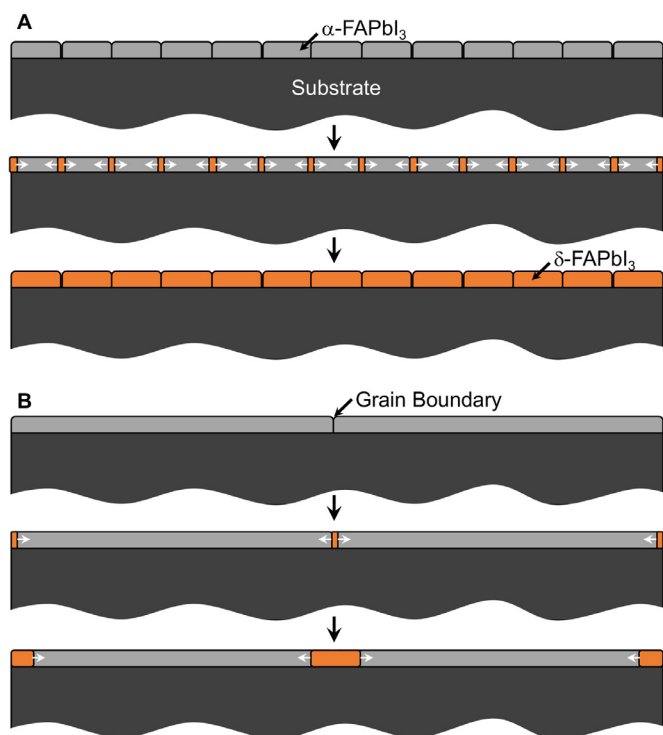


**Fig. 9.** Cross-sectional schematic illustrations depicting the effect of grain-boundary density in  $\alpha$ -FAPbI<sub>3</sub> thin films (cross-section) on the progression of  $\alpha$ -to- $\delta$  reverse transformation induced by the inward ingress of moisture through grain boundaries and lateral growth of the transformation front: (A) medium-grained ( $d \sim 1.2 \mu\text{m}$ ) and (B) ultra-coarse-grained ( $d \sim 7.6 \mu\text{m}$ ). Approximately to scale.

thin film compared to the ultra-coarse-grained thin film, as depicted in the idealized, but to-scale, cross-sectional schematic diagrams in Fig. 9A and 9B, respectively. Thus, a significantly lower grain-boundary density in the ultra-coarse-grained  $\alpha$ -FAPbI<sub>3</sub> thin film is responsible for its dramatically improved stability in humid environment.

While the improvements in the PV performance of PSCs with ultra-coarse-grained  $\alpha$ -FAPbI<sub>3</sub> OIHP thin films, is measurable, it is somewhat modest. This can be attributed to ‘invisible’ sub-grain boundaries within the otherwise single-crystal  $\alpha$ -FAPbI<sub>3</sub> grains can also block photocarriers as effectively as regular grain boundaries, as shown in our recent optical-characterization studies [33,34]. It is worth noting that the discovery of that effect was made possible by our ability to grow such large grains in  $\alpha$ -FAPbI<sub>3</sub> OIHP, where individual grains could be probed accurately within the spatial-resolution limitations of optical-characterization techniques [33,34]. Unlike regular grain boundaries, it is unlikely that these sub-grain boundaries allow facile ingress of H<sub>2</sub>O. Also, as mentioned earlier, the use of naturally occurring grain-boundary grooves to represent the grain boundaries (*i.e.* not etched) is non-conservative [6,30,38]. Thus, the effective ‘grain size’ relevant to photocarriers, but not necessarily to environmental stability, is likely to be smaller than that measured here.

The improved environmental stability of ultra-coarse-grained  $\alpha$ -FAPbI<sub>3</sub> OIHP would translate into improved stability of the PSCs made from these thin films, provided the overall PSCs stability is not dominated by the stability of the other layers and the interfaces within the PSCs. While future commercial PSCs incorporating OIHP thin films will always be encapsulated (hermetically sealed), there is a need for the OIHP to be inherently stable in the ambient environment to assure overall stability of the PSCs that are expected to operate reliably for years. This is particularly important in the case of flexible PSCs for potential applications such as portable chargers, tents, backpacks, deployable rollups, drones, *etc.*, where achieving

‘perfect’ encapsulation is problematic. As such, the approach for stabilizing  $\alpha$ -FAPbI<sub>3</sub> via exceptional grain-coarsening demonstrated here is inherently attractive. Also, this approach could be coupled with other recently reported approaches mentioned earlier: surface functionalization [24], grain-boundary functionalization [25,26], and doping [27].

## 5. Conclusions

The following conclusions can be drawn from this study.

- DMSO solvent-vapor plays a unique role in promoting  $\delta$ -to- $\alpha$  FAPbI<sub>3</sub> transformation in thin films ( $\sim 300 \text{ nm}$  thickness) at a relatively low temperature ( $\sim 95 \text{ }^\circ\text{C}$ ), and results in an ultra-large-grained (up to  $\sim 9 \mu\text{m}$ )  $\alpha$ -FAPbI<sub>3</sub> thin-film microstructure.
- The polar DMSO molecules interact with  $\delta$ -FAPbI<sub>3</sub> thin film electrostatically, and appear to lower the activation energy for the reconstructive  $\delta$ -to- $\alpha$  transformation.
- Vapors of solvents with lower PI values (NMP and DMF) are less effective in promoting the  $\delta$ -to- $\alpha$  transformation, and attendant grain growth, which indicates weaker interaction with the  $\delta$ -FAPbI<sub>3</sub> thin film. This supports the hypothesis that FAPbI<sub>3</sub>-vapor interaction is primarily electrostatic in nature.
- Reduction in activation energy facilitated by the DMSO solvent-vapor results in faster  $\delta$ -to- $\alpha$  phase transformation at a relatively low temperature where the nucleation rate is suppressed. The few nuclei grow rapidly to result in the ultra-coarse-grained microstructure.
- The reverse  $\alpha$ -to- $\delta$  transformation phase transformation in FAPbI<sub>3</sub> thin films exposed to humid environment appears to be related to H<sub>2</sub>O ingress along grain boundaries. Consequently, the ultra-coarse-grained  $\alpha$ -FAPbI<sub>3</sub> thin films with low grain-boundary density show dramatically superior phase stability compared to  $\alpha$ -FAPbI<sub>3</sub> thin films with smaller grain sizes.
- PCE of the ‘champion’ PSC fabricated using ultra-coarse-grained  $\alpha$ -FAPbI<sub>3</sub> thin films exceeds 19%, and the average PCE is measurably higher than that of PSCs fabricated with medium-grained  $\alpha$ -FAPbI<sub>3</sub> thin films. However, this PCE improvement is modest, which can be attributed to the photocarriers-blocking at sub-grain boundaries in ultra-coarse-grained  $\alpha$ -FAPbI<sub>3</sub> thin films.

## Declaration of Competing Interest

The authors declare that they have no known competing financial interests or personal relationships that could have appeared to influence the work reported in this paper.

## Acknowledgments

This research was supported by the Office Naval Research (grant no. N00014-17-1-2232), with additional funding from the National Science Foundation (grant nos. OIA-1538893 and OIA-1929019). The experimental assistance from M. Chen and H.F. Garces is gratefully acknowledged.

## Supplementary materials

Supplementary material associated with this article can be found in the online version at doi:10.1016/j.actamat.2020.03.036.

## References

- [1] N.-G. Park, M. Grätzel, T. Miyasaka, *Organic-Inorganic Halide Perovskite Photovoltaics: From Fundamentals to Device Architectures*, Springer, Zurich, Switzerland, 2016.

- [2] H.J. Snaith, Present status and future prospects of perovskite photovoltaics, *Nat. Mater.* 17 (2018) 372–376.
- [3] A.K. Jena, A. Kulkarni, T. Miyasaka, Halide perovskite photovoltaics: Background, status, and future prospects, *Chem. Rev.* 119 (2019) 3026–3103.
- [4] A. Kojima, K. Teshima, Y. Shirai, T. Miyasaka, Organometal halide perovskites as visible-light sensitizers for photovoltaic cells, *J. Am. Chem. Soc.* 131 (2009) 6050–6051.
- [5] NREL, <https://www.nrel.gov/pv/cell-efficiency.html> (2019)
- [6] W.A. Dunlop-Shohl, Y. Zhou, N.P. Padture, D.B. Mitzi, Synthetic approaches for halide perovskite thin films, *Chem. Rev.* 119 (2019) 3193–3295.
- [7] D.B. Mitzi, Synthesis, structure, and properties of organic-inorganic perovskites and related materials, in: K.D. Karlin (Ed.), *Progress in Inorganic Chemistry*, 48, John Wiley & Sons, New York, NY, 1999.
- [8] B. Saparov, D.B. Mitzi, Organic-inorganic perovskites: Structural versatility for multifunctional materials design, *Chem. Rev.* 116 (2016) 4558–4596.
- [9] G.E. Eperon, S.D. Stranks, C. Menelaou, M.B. Johnston, L.M. Herz, H.J. Snaith, Formamidinium lead trihalide: A broadly tunable perovskite for efficient planar heterojunction solar cells, *Ener. Environ. Sci.* 7 (2014) 982–988.
- [10] T. Chen, B.J. Foley, C. Park, C.M. Brown, L.W. Harringer, J. Lee, J. Ruff, M. Yoon, J.J. Choi, S.-H. Lee, Entropy-driven structural transition and kinetic trapping in formamidinium lead iodide perovskite, *Sci. Adv.* 2 (2016) e1601650.
- [11] V.L. Pool, B. Dou, D.G. van Campen, T.R. Klein-Stockert, F.S. Barnes, S.E. Shaheen, M.I. Ahmad, M.F.A.M. van Hest, M.F. Toney, Thermal engineering of FAPbI<sub>3</sub> perovskite material via radiative thermal annealing and *in situ* XRD, *Nat. Commun.* 8 (2017) 14075.
- [12] Y. Zhou, J. Kwun, H.F. Garces, S. Pang, N.P. Padture, Observation of phase-retention behavior of the HC(NH<sub>2</sub>)<sub>2</sub>PbI<sub>3</sub> black perovskite polymorph upon mesoporous TiO<sub>2</sub> scaffolds, *Chem. Commun.* 52 (2016) 7273–7275.
- [13] Q. Han, S.-H. Bae, P. Sun, Y.-T. Hsieh, Y. Yang, Y.S. Rim, H. Zhao, Q. Chen, W. Shi, G. Li, Y. Yang, Single crystal formamidinium lead iodide (FAPbI<sub>3</sub>): Insight into the structural, optical, and electrical properties, *Adv. Mater.* 28 (2016) 2253–2258.
- [14] S. Adjokatse, H.-H. Fang, H. Duim, M.A. Loi, Scalable fabrication of high-quality crystalline and stable FAPbI<sub>3</sub> thin films by combining doctor-blade coating and the cation exchange reaction, *Nanoscale* 11 (2019) 5989–5997.
- [15] J.S. Yun, J. Kim, T. Young, R.J. Patterson, D. Kim, J. Seidel, S. Lim, M.A. Green, S. Huang, A. Ho-Baillie, Humidity-induced degradation via grain boundaries of HC(NH<sub>2</sub>)<sub>2</sub>PbI<sub>3</sub> planar perovskite solar cells, *Adv. Funct. Mater.* 28 (2018) 1705363.
- [16] N.J. Jeon, J.H. Noh, W.S. Yang, Y.C. Kim, S. Ryu, J. Seo, S.I. Seok, Compositional engineering of perovskite materials for high-performance solar cells, *Nature* 517 (2015) 476–480.
- [17] Z. Li, M. Yang, J.-S. Park, S.-H. Wei, J.J. Berry, K. Zhu, Stabilizing perovskite structures by tuning tolerance factor: Formation of formamidinium and cesium lead iodide solid-state alloys, *Chem. Mater.* 28 (2016) 284–292.
- [18] M. Saliba, T. Matsui, J.-Y. Seo, K. Domanski, J.-P. Correa-Baena, M.K. Nazeeruddin, S.M. Zakeeruddin, W. Tress, A. Abate, A. Hagfeldt, M. Grätzel, Cesium-containing triple cation perovskite solar cells: Improved stability, reproducibility and high efficiency, *Energy & Environ. Sci.* 9 (2016) 1989–1997.
- [19] S.H. Turren-Cruz, A. Hagfeldt, M. Saliba, Methylammonium-free, high-performance, and stable perovskite solar cells on a planar architecture, *Science* 362 (2018) 449–453.
- [20] A. Amat, E. Mosconi, E. Ronca, C. Quarti, P. Umari, M.K. Nazeeruddin, M. Grätzel, F.D. Angelis, Cation-induced band-gap tuning in organohalide perovskites: Interplay of spin-orbit coupling and octahedra tilting, *Nano Lett.* 14 (2014) 3608–3616.
- [21] Y. Zhou, Z. Zhou, M. Chen, Y. Zong, J. Huang, S. Pang, N.P. Padture, Doping and alloying for improved solar cells, *J. Mater. Chem. A* 4 (2016) 17623–17635.
- [22] C.C. Boyd, R. Cheacharoen, T. Leijtens, M.D. McGehee, Understanding degradation mechanisms and improving stability of perovskite photovoltaics, *Chem. Rev.* 119 (2019) 3418–3451.
- [23] L. Gu, D. Zhang, M. Kam, Q. Zhang, S. Poddar, Y. Fu, X. Mo, Z. Fan, Significantly improved black phase stability of FAPbI<sub>3</sub> nanowires via spatially confined vapor phase growth in nanoporous templates, *Nanoscale* 10 (2018) 15164–15172.
- [24] Y. Fu, T. Wu, J. Wang, J. Zhai, M.J. Shearer, Y. Zhao, R.J. Hamers, E. Kan, K. Deng, X.-Y. Zhu, S. Jin, Stabilization of the metastable lead iodide perovskite phase via surface functionalization, *Nano Lett.* 17 (2017) 4405–4414.
- [25] J.-W. Lee, Z. Dai, C. Lee, H.M. Lee, T.-H. Han, N.D. Marco, O. Lin, C.S. Choi, B. Dunn, J. Koh, D.D. Carlo, J.H. Ko, H.D. Maynard, Y. Yang, Tuning molecular interactions for highly reproducible and efficient formamidinium perovskite solar cells via adduct approach, *J. Am. Chem. Soc.* 140 (2018) 6317–6324.
- [26] T. Niu, J. Lu, M.-C. Tang, D. Barrit, D.-M. Smilgies, Z. Yang, J. Li, Y. Fan, T. Luo, I. McCulloch, A. Amassian, S. Liu, K. Zhao, High performance ambient-air-stable FAPbI<sub>3</sub> perovskite solar cells with molecule-passivated Ruddlesden-Popper/3D heterostructured film, *Energy Environ. Sci.* 11 (2018) 3358–3366.
- [27] H. Min, M. Kim, S.-U. Lee, H. Kim, G. Kim, K. Choi, J.H. Lee, S.I. Seok, Efficient, stable solar cells by using inherent bandgap of  $\alpha$ -phase formamidinium lead iodide, *Science* 366 (2019) 749–753.
- [28] S.K. Yadavalli, Y. Zhou, N.P. Padture, Exceptional grain growth in formamidinium lead iodide perovskite thin films induced by the  $\delta$ -to- $\alpha$  phase transformation, *ACS Energy Lett.* 3 (2018) 63–64.
- [29] C.V. Thompson, Grain growth in thin films, *Ann. Rev. Mater. Sci.* 20 (1990) 245–268.
- [30] Y. Zhou, O.S. Game, S. Pang, N.P. Padture, Microstructures of organometal trihalide perovskites for solar cells: Their evolution from solutions and characterization, *J. Phys. Chem. Lett.* 6 (2015) 4827–4839.
- [31] Q. Wang, B. Chen, Y. Liu, Y. Deng, Y. Bai, Q. Dong, J. Huang, Scaling behavior of moisture-induced grain degradation in polycrystalline hybrid perovskite thin films, *Energy Environ. Sci.* 10 (2017) 516–522.
- [32] Y. Yuan, J. Huang, Ion migration in organometal trihalide perovskite and its impact on photovoltaic efficiency and stability, *Acc. Chem. Res.* 49 (2016) 286–293.
- [33] W. Li, S. Yadavalli, D. Lizarazo-Ferro, M. Chen, Y. Zhou, N.P. Padture, R. Zia, Sub-grain special boundaries in halide perovskite thin films restrict carrier diffusion, *ACS Energy Lett.* 3 (2018) 2669–2670.
- [34] W. Li, M.S.R. Huang, S.K. Yadavalli, D. Lizarazo-Ferro, Y. Zhou, A. Zaslavsky, N.P. Padture, R. Zia, Direct characterization of carrier diffusion in halide-perovskite thin films using transient photoluminescence imaging, *ACS Photon.* 6 (2019) 2375–2380.
- [35] N.J. Jeon, J.H. Noh, Y.C. Kim, W.S. Yang, S. Ryu, S.I. Seok, Solvent engineering for high-performance inorganic-organic hybrid perovskite solar cells, *Nat. Mater.* 9 (2014) 897–903.
- [36] Z.G. Xiao, Q.F. Dong, C. Bi, Y.C. Shao, Y.B. Yuan, J.S. Huang, Solvent annealing of perovskite-induced crystal growth for photovoltaic-device efficiency enhancement, *Adv. Mater.* 26 (2014) 6503–6509.
- [37] T.A. Skotheim, J. Reynolds, *CRC handbook of Conducting Polymers*, CRC Press, Boca Raton, FL, 2007.
- [38] S. Jariwala, H. Sun, G.W.P. Adhyaksa, A. Lof, L.A. Muscarella, B. Ehrler, E.C. Garnett, D.S. Ginger, Local crystal misorientation influences non-radiative recombination in halide perovskites, *Joule* 3 (2019) 3048–3060.
- [39] D.W. Readey, *Kinetics in Materials Science and Engineering*, CRC Press, Boca Raton, FL, 2017.
- [40] Q. Dong, J. Li, Y. Shi, M. Chen, L.K. Ono, K. Zhou, C. Zhang, Y. Qi, Y. Zhou, N.P. Padture, L. Wang, Improved SnO<sub>2</sub> electron transport layers solution-deposited at near room temperature for rigid or flexible perovskite solar cells with high efficiencies, *Adv. Ener. Mater.* 9 (2019) 1900834.
- [41] Y. Jo, K.S. Oh, M. Kim, K.-H. Kim, H. Lee, C.-W. Lee, D.S. Kim, High performance of planar perovskite solar cells produced from PbI<sub>2</sub>(DMSO) and PbI<sub>2</sub>(NMP) complexes by intramolecular exchange, *Adv. Mater. Interf.* 3 (2016) 1500768.
- [42] J. Liu, C. Gao, X. He, Q. Ye, L. Ouyang, D. Zhuang, C. Liao, J. Mei, W. Lau, Improved crystallization of perovskite films by optimized solvent annealing for high efficiency solar cell, *ACS Appl. Mater. Interf.* 7 (2015) 24008–24015.
- [43] W.M. Haynes, *CRC Handbook of Chemistry and Physics*, CRC Press, Boca Raton, FL, 2011.
- [44] F. Liu, F. Sommer, C. Bos, E.J. Mittemeijer, Analysis of solid state phase transformation kinetics: Models and recipes, *Int. Mater. Rev.* 52 (2007) 193–212.
- [44] S. Prathapani, D. Choudhary, S. Mallick, P. Bhargava, A. Yella, Experimental evaluation of room temperature crystallization and phase evolution of hybrid perovskite materials, *CrystEngComm* 19 (2017) 3834–3843.